Chemical Engineering Journal 480 (2024) 147936

Contents lists available at ScienceDirect

Chemical Engineering Journal

journal homepage: www.elsevier.com/locate/cej

Engineering heterogeneous domains and interfaces in shape memory fibers for tunable responsive behaviors

Zhongkun Zhao [a], Haoqing Yang [a], Manqi Li [b], Chandan Gudi [a], Kamal Varma Kanumuru [a], Robert Voigt [a], Olalekan Babaniyi [c], Tengxiao Liu [d,*], Yong Chen [b,e,*], Hongtao Sun [a,f,*]

[a] The Harold & Inge Marcus Department of Industrial & Manufacturing Engineering, Pennsylvania State University, University Park, PA 16802, USA
[b] Department of Aerospace and Mechanical Engineering, University of Southern California, Los Angeles, CA 90089, USA
[c] School of Mathematical Sciences, Rochester Institute of Technology, Rochester, NY 14623, USA
[d] Department of Biomedical Engineering, Pennsylvania State University, University Park, PA 16802, USA
[e] Epstein Department of Industrial and Systems Engineering, University of Southern California, Los Angeles, CA 90089, USA
[f] Materials Research Institute (MRI), Pennsylvania State University, University Park, PA 16802, USA

ARTICLE INFO

Keywords:
3D printing
Shape memory polymer
Heterogeneities
Interfaces
Torsional actuator
Digital image correlation

ABSTRACT

Intelligent materials have rapidly evolved to enable sensing and responding to various external stimuli, opening exciting opportunities across various fields such as soft robotics, actuators, biomedical devices, and sensors. Among these materials, Shape Memory Polymers (SMPs) have gained prominence for their unique shape memory effects and deformable properties. However, achieving effective control over these responsive behaviors remains a scientific challenge. To address this challenge, we present a novel strategy that involves creating heterogeneous domains and finely controlling interfaces within a single SMP material. Our approach leverages grayscale lithography-enabled printing, which facilitates the regulation of transition interfaces and orientations between relatively stiff and elastic domains within a fiber-shaped actuator. These deliberately designed heterogeneities give rise to tunable thermal stimuli-responsive behaviors and torsional mechanical energy. Our strategy, characterized by the manipulation of heterogeneous domains and their transition interfaces, opens a pioneering avenue for designing and fabricating intelligent materials and associated actuation devices.

1. Introduction

Intelligent materials have gained extensive utilization in various fields, including soft robotics, smart textiles, biomimetic machines, actuators, and powered exoskeletons [1–7]. Shape memory polymers (SMPs), one of the most attractive intelligent soft materials, have received intense interest due to their synthetic flexibility and stimuli-responsive deformation. A wide range of SMPs, including amorphous polymers [8,9], semicrystalline polymers [10,11], liquid crystalline elastomers (LCE) [12], and hydrogels [13–17], have been developed to offer unique properties and functionalities. The SMPs can be programmed to adopt a temporary shape by applying external force when heated to a high temperature (T_d), typically near the glass transition temperature (T_g). Once quenched at room temperature, the temporary shape becomes fixed. Remarkably, when the programmed SMPs are subsequently reheated, they recover their original shape in response to thermal stimuli. This unique shape-memory effect empowers SMPs to generate programmable movements, including bending, twisting, and contraction, in response to external stimuli [18–22]. Particularly, fiber-shaped SMPs enable a lightweight actuator with a superior power-to-mass ratio, extensive strains, and high responsiveness [23–30]. By applying a twist or coiled structure [31], the fiber-shaped actuators function as torsional or tensile artificial muscles, exhibiting exceptional work capacity and responsiveness. These actuators can achieve an energy density 50 times higher than that of natural human muscles, enabling them to lift loads over 600 times their weight [32,33].

Nonetheless, the precise modulation of material properties and responsive behaviors in synthetic intelligent materials remains a formidable scientific challenge. A potential solution lies in the strategic design of site-specific local properties, thus engendering multifaceted benefits within a single material for the regulation of global properties. In this context, the incorporation of heterogeneous domains, such as

* Corresponding authors at: Department of Aerospace and Mechanical Engineering, University of Southern California, Los Angeles, CA 90089, USA (Y. Chen); The Harold & Inge Marcus Department of Industrial & Manufacturing Engineering, Pennsylvania State University, University Park, PA 16802, USA (H. Sun).
E-mail addresses: tql5160@psu.edu (T. Liu), yongchen@usc.edu (Y. Chen), hongtao.sun@psu.edu (H. Sun).

https://doi.org/10.1016/j.cej.2023.147936
Received 6 September 2023; Received in revised form 2 December 2023; Accepted 5 December 2023
Available online 8 December 2023

functional graded structures/materials, emerges as a viable avenue, albeit necessitating sophisticated manufacturing techniques. However, current approaches such as electrospinning and wet spinning often possess limited control over heterogeneities within a single material [1,34]. To surmount these limitations, the advent of three-dimensional (3D) printing-based photo stereolithography stands out as a promising solution. This technique empowers the encoding of photo-sensitive resins with spatially regulated material properties and responsive performance in the final products, extending beyond mere control of the printed geometry. The photo stereolithography process, which involves dynamic mask application, facilitates the precise adjustment of local material properties and heterogeneities by manipulating curing times spatially [35]. Through the spatiotemporal modulation of UV light, this 3D printing approach offers a potential avenue for the design and fabrication of heterogeneous structures within a single material. In doing so, it expands the possibilities in material design and fabrication [36–38].

In this study, we employ a photo-stereolithography-enabled 3D printing technique to exert effective control over the thermal-responsive performance and stored mechanical energy of fiber-shaped SMP actuators. Our innovative approach involves the design and incorporation of heterogeneous domains and interfaces, enabling the regulation of shape-memory characteristics within a single torsional actuator. We first focus on the fundamental investigations to establish correlations between UV curing times and corresponding material behaviors (such as mechanical properties and thermal-responsive rotations) in 3D-printed homogeneous SMP fibers. By manipulating curing times during the 3D printing process, the resulting homogeneous actuators exhibit an adjustable elastic modulus from 524 to 928 MPa, along with controlled torsional movements that yield peak rotation speeds ranging from 109 to 314 rpm. Drawing from these curing time-dependent properties, we have developed a grayscale lithography approach. Leveraging a photo-stereolithography-based LCD 3D printer, this technique empowers the spatiotemporal control of site-specific photo-polymerization, enabling the creation of heterogeneous domains with different features. Specifically, this capability is advantageous for interface design, allowing for features such as abrupt transitions or gradient transitions between distinct domains, as opposed to a simple integration of dissimilar materials/components into one structure [37]. Consequently, we can seamlessly incorporate heterogeneous domains within a single SMP actuator. To comprehensively understand the mechanisms underlying tunable thermal stimuli-responsive behaviors and torsional mechanical energy, we investigated the local mechanical properties associated with various heterogeneous domains using the digital imaging correlation (DIC) methodology. Our innovative grayscale photo-lithography-enabled printing process provides a general strategy for designing and fabricating various functional and structural polymers using UV curable precursor resins. For example, this approach has already shown promise in encoding other thermal responsive hydrogels, enabling the creation of intricate bioinspired 3D structures, as well as programmable shape morphing and sequential motions [39,40]. Its applications extend to soft robotics, biomimetic manufacturing, and other fields.

2. Material and methods

2.1. Material preparation

Methyl acrylate (MA), isobornyl acrylate (IBOA), 1,6-hexanediol diacrylate (HDDA), Bis(2,4,6-trimethylbenzoyl)-phenylphosphineoxide (Irgacure 819), methanol, and ethyl acetate were obtained from Sigma-Aldrich (USA) and used as purchased. MA (56.9 mol%) and IBOA (40.3 mol%) as comonomers, HDDA (2.8 mol%) as a crosslinker, and Irgacure819 (0.5 wt%) as the photoinitiator were mixed at room temperature and stirred for 6 h to create the printing precursor. The precursor was stored away from light before printing to prevent property deterioration.

2.2. Printing system setup and printing procedure of SMP fibers

The layer-by-layer 3D printing of shape memory polymer fibers was achieved using a liquid crystal display (LCD) 3D printer (Anycubic Photon Mono X 6 K, Shenzhen, China). A fixed-height digital light curing system was developed for grayscale lithography. A closed printing cell was constructed using a vat, two fixed-height cover glasses (height: 0.6–0.9 mm), and a large cover glass on top (Fig. S16). CAD software (Solidworks) was employed for designing the printing models. It is important to note that the curing thickness of the specimen is fixed during our fixed-height printing process. The various thicknesses indicated in the printing models do not represent the dimensions of the printing samples. Instead, they signify the number of repeated curing times (25 s for each unit exposure), which can tune the material properties by varying the accumulated doses of UV exposure. For instance, within the same fixed height, a region with a 150 s curing time required six-unit UV exposures (6×25 s per layer = 150 s), while a region with a 50 s curing time needed to be exposed twice (2×25 s per layer = 50 s).

To fabricate the SMP fibers for torsional rotation demonstration, the printing precursor was injected into the closed cell and cured by the LCD printer, resulting in fibers with dimensions of 0.9×0.9×120 mm. Smaller dimensions (*e.g.*, 0.6×0.6×35 mm) of the printed fibers were obtained for measuring the stored and released mechanical energy. Following the printing process, a post-printing washing step was conducted using a solvent mixture of ethyl acetate and methanol (ratio 1:1) to remove any excess unreacted monomers present in the printed samples. Subsequently, the samples were heated in an oven at 100 °C for 15 min.

2.3. Characterizations and measurements

The glass transition temperature of the as-printed fibers from layer-by-layer printing was determined using a dynamic mechanical analyzer (DMA, Q800 TA Instruments) (temperature range: 20 °C – 100 °C; heating rate: 5 °C min^{-1}; frequency: 1 Hz). DMA was also employed to measure the torque, storage modulus, loss modulus, and tan δ at specific temperatures. DMA (Anton Paar MCR 702e) was used for the measurement of glass transition temperature (T_g) of homogenous and heterogenous SMP fibers (dimension: 0.6×0.6×35 mm) (temperature: 30 to 100 °C; heating rate: 2 °C min^{-1}; frequency: 1 Hz; oscillating amplitude: 0.01 % strain).

The mechanical properties, including Young's modulus, strain at break, ultimate tensile stress, and yield point, were obtained using a mechanical tester (CS2-1100 Series, Chatillon) through the tensile test. Young's modulus values were calculated from the slope of each stress-strain curve, and ultimate tensile stress values were obtained from the maximum value in each stress-strain curve. The yield points were obtained from the interception among the 0.2 % offset lines and the stress-strain curves. Tensile toughness can be calculated using the area underneath the stress–strain curve. Dog-bone specimens (with a middle cross-sectional area: 0.5×5 mm) printed using the same SMP were stretched at a constant strain rate of 2 mm min^{-1} at room temperature.

A custom-built torsion tester (M7I, Mark-10) was utilized to measure the torque at room temperature and demonstrate the stimuli-responsive rotation motion and work capacity at T_g. The test platform consists of a programmable step motor, a sensor, a heating band, and a temperature controller. This comprehensive setup allows for the generation of rotation motion, torque measurement, and precise control of the environmental temperature surrounding the tested samples. For the torque measurements, the layer-by-layer printed fiber (dimension: 1.5 mm × 1.5 mm × 120 mm) was rotating with one end tethered and connected to the torque sensor, and the other end driven by a step motor. To calculate the shear modulus of the SMP fibers, the shear strain and shear stress are given by: $\gamma_{xy} = R_s\frac{\theta}{L_s}$, and $\tau_{xy} = \Gamma/(\frac{\pi R_s^3}{2})$, respectively, where R_s is the radius of fiber, L_s is its length. The torque Γ and twisted angle θ were

directly measured through twisting tests. From the curves of shear stress versus shear strain at small twist angles (strain <0.02), the shear modulus can be derived from the slope for each curve. For the rotation demonstration, a fiber was tethered between two grippers and then subjected to heat using the heating band, reaching the desired temperature (T_d). The fiber could be programmatically twisted to different degrees or turns during this process. Subsequently, the SMP fiber was quenched to room temperature, fixing its twisted state. The fiber could revert to its original untwisted state when reheating to T_d. A 1.5 g load was subjected to one end of the fiber.

DMA (Anton Paar MCR 702e) was employed to measure the torque (three heterogeneous fibers as rotating motors and two homogeneous motors as loads), as well as the work capacity of heterogeneous fibers in a two-part hybrid fiber (total length: 7 cm). The upper region (3.5 cm in length) serves as a rotating motor, while the lower region (3.5 cm in length), acts as a torsional load. The upper motor can rotate and overcome the increasing torsional load generated by the lower region as it continues to be twisted, thereby delivering work capacity. The number of turns and rotating speed of the lower load region, driven by the upper motor region, were determined through frame-by-frame vi. deo recording. The released mechanical energy of the rotating motor was obtained by integrating the torque-angle curves using the formula $U = \Gamma \int d\theta$, where Γ and θ represent the measured torque and rotation angle of the torsional load part, respectively. The power of the motor part was calculated using the formula P = U/t. The mass of the load part was 0.02 g, allowing for the calculation of specific energy density and specific power density.

Digital image correlation (DIC) analysis was used as a non-contact, non-interferometric method to measure the complete information of deformation or strain mapping of SMP samples. This technique utilizes a stereoscopic camera setup to capture a series of digital images of the deforming surface during the tensile test. The surface strain can be determined through correlation analysis by comparing the measured surface contour with the resolved displacement from the image sequence. To perform DIC analysis, a reference image of the undeformed surface is acquired before the test. Random patterns are applied to the measuring surface, serving as markers for correlation. These patterns are tracked and compared with those in the reference state to calculate the displacement and strain. In this study, graphene oxide powders with a size range of 15–20 μm were mixed with the precursor resin before printing, allowing them to act as markers for DIC. The tensile tests were conducted at a frequency of 2 Hz, and the time-resolved optical images were captured using the ARAMIS 12 M sensor. The strain mappings and associated analysis were obtained from GOM Correlate software.

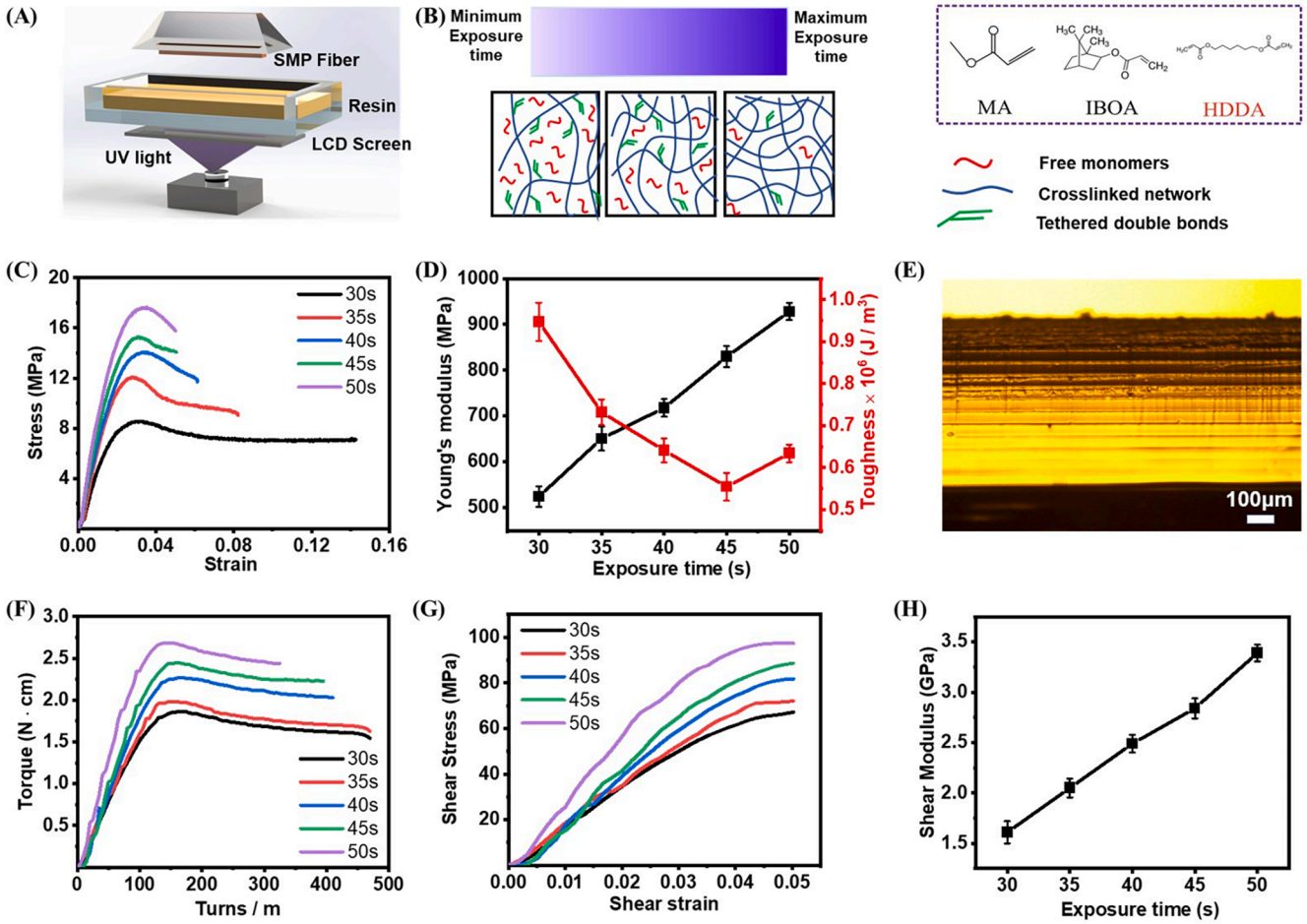

Fig. 1. Mechanical behaviors of SMP fibers at different exposure times. A) Schematic illustration of the photo-stereolithography-enabled 3D printing. B) Schematic illustration of exposure-time-dependent curing behaviors and chemical structures of photo-sensitive precursors. C) Stress-strain curves of SMP fibers exposed under different exposure times (*e.g.*, 30, 35, 40, 45, 50 s) at room temperature. D) Young's modulus and toughness versus exposure time. E) Optical microscope image of a cross-sectional view of SMP fiber. F) The torque needed to twist the SMP exposed under different exposure times (30–50 s) at room temperature. G) Shear stress versus shear strain at low twist strains. H) Shear modulus versus exposure time.

3. Results and discussion

3.1. Effect of UV curing time on mechanical properties of SMP fibers via layer-by-layer printing

The variation in curing time enables us to regulate the mechanical properties of SMP fibers. In Fig. 1A, we present a "bottom-up" configuration of a photo-stereolithography-based LCD 3D printing technique, which employs UV light to trigger the photo-polymerization reaction in a layer-by-layer manner. Specifically, our photo-sensitive precursors consist of methyl acrylate (MA 56.9 mol%), isobornyl acrylate (IBOA 40.3 mol%) as comonomers, 1,6-hexanediol diacrylate (HDDA 2.8 mol %) as a crosslinker, and bis (2,4,6-trimethyl benzoyl)-phenylphosphineoxide (Irgacure819 0.5 wt%) as a photoinitiator. When exposed to UV light, the photoinitiator in the precursor resin converts photolytic energy into reactive species, initiating polymerization. Specifically, the photoinitiator undergoes cleavage to produce free radicals, which then propagate to attack other monomers. These triggered monomers facilitate chain growth and crosslinking during polymerization [41,42]. It is important to note that at this stage, different exposure times correspond to varying levels of photolytic energy absorptions, which, in turn, influences the photo-polymerization process in the printed polymers (Fig. 1B). To further investigate the UV curable properties, we conducted a series of layer-by-layer printing using five different exposure times (30, 35, 40, 45, and 50 s) to fabricate fiber-shaped SMP actuators. The printing dimensions are summarized in Table S1. Quantitative mechanical characterizations were performed by measuring the stress required to stretch and the torque needed to twist the fibers at room temperature. Specifically, the stress − strain curves of the as-printed SMP fibers under various exposure times were obtained through uniaxial tensile tests, revealing variations in ultimate strength and strain at the point of failure based on the exposure time (Fig. 1C). For instance, the fiber printed with an exposure time of 30 s exhibited an ultimate strength of 8 MPa, which monotonically increased to 18 MPa as the exposure time increased to 50 s. A similar variation was observed for Young's modulus, obtained from the slope of the linear region of stress-strain curves, ranging from 524 to 928 MPa, as the exposure time varied from 30 to 50 s. To elucidate the trade-off between high modulus and high toughness, we plotted Young's modulus and toughness of the SMP fibers at various exposure times (Fig. 1D). The fiber with the shortest exposure time of 30 s displayed the highest toughness of 0.95×10^6 J m^{-3} but the lowest Young's modulus of 524 MPa. As the exposure time increased to the maximum exposure time of 50 s, the toughness decreased to 0.63×10^6 J m^{-3}, while Young's modulus reached its maximum value of 928 MPa. These findings provide insight into the relationship among exposure time, Young's modulus, and toughness in the as-printed homogeneous SMP fibers.

The optical microscope image in Fig. 1E illustrates the cross-sectional view of the as-printed fiber and indicates a layered texture attributed to layer-by-layer printing. The thickness of each layer is consistent with the printing layer thickness (~50 μm). In addition to tensile tests, we also investigated torsion tests, and the results are illustrated in Fig. 1F. A single fiber (dimension: 1.5 mm × 1.5 mm × 120 mm) requires greater torque to twist when printed under a longer curing time per layer. Assuming SMP fibers as non-coiled cylinders, the shear strain and shear stress are given by: $\gamma_{xy} = R_s\frac{\theta}{L_s}$, and $\tau_{xy} = \Gamma/(\frac{\pi R_s^3}{2})$, respectively, where R_s is the radius of fiber, L_s is its length. The torque Γ and twisted angle θ were directly measured through twisting tests. From the curves of shear stress versus shear strain at small twist angles (strain <0.02), the shear modulus can be derived from the slope for each curve, as shown in Fig. 1G. Increasing the exposure time also boosts the shear modulus of SMP fibers, allowing them to sustain a higher torque under twist, as demonstrated in Fig. 1H. Therefore, the mechanical properties of our 3D-printed SMP fibers can be widely tuned by varying the curing time during layer-by-layer 3D printing.

3.2. Thermal responsive rotation behaviors of homogeneous fiber-shaped actuators via layer-by-layer printing

Furthermore, we assessed the shape memory effect through a rotational motion to demonstrate the performance of SMP fibers as soft micro-motors in response to heat stimuli. The key parameters characterizing the rotation motion, such as rotation turns and rate, were used for this purpose. A custom-built platform integrating a stepper motor, a torque/force sensor, a heating band, and a temperature controller was employed. This setup allowed us to generate rotation motion, measure torque, and control the environmental temperature surrounding the tested samples (Fig. 2A). When the heating temperature (T_d) exceeded the glass transition temperature T_g (72 °C), the SMP fibers transitioned from a glassy state to a rubbery state. Under external force, the randomly wound molecular chains in the SMP could be deformed. To initiate the experiment, the as-printed fibers were first twisted at a programming temperature T_d (75 °C), for 200 turns per meter (*e.g.*, 20 turns for 10-cm SMP fiber), and their torsional mechanical energy was stored upon quenching back to room temperature (Fig. 2A). Upon reheating to T_d, the melting of the crystalline phase resulted in the softening of the SMP materials, causing the deformed molecular chains to revert to their original winding structure. Consequently, the twisted fibers underwent untwisting, producing a rotation motion akin to a micromotor.

The glass transition temperature (T_g) of our SMPs can be tuned by adjusting the formulation of the resin. Our resin precursor consists of MA and IBOA comonomers with similar acrylate-based reactivities. However, their homopolymers after polymerization exhibit drastically different glass transition temperatures (*e.g.*, 9 °C and 85 °C). Thus, by regulating the ratio of comonomers MA and IBOA, it becomes possible to control the glass transition temperature of the resulting SMP [35]. For instance, adjusting the molar ratio to 0.71 (IBOA/MA) allows for the regulation of the as-printed SMP's glass transition temperature to approximately 72 °C, as determined by dynamic mechanical analysis (DMA) (Fig. S1). Similarly, adjusting the ratio to 0.62 (IBOA/MA) decreases the glass transition temperature to 50 °C (Fig. S1). Moreover, when varying the curing time from 30 to 50 s, the T_g values exhibit only marginal fluctuations within a limited range (Figs. S2-S6).

During the untwisting motion, all SMP fibers were subjected to a 1.5 g weighted load, which is 30 times the weight of the fiber. The time-resolved free rotation, specifically the untwisting motion, of the SMP fibers was measured when programming for 200 turns m^{-1}, as shown in Fig. 2B. The rotation rate (rpm) was calculated based on the first derivative of the correlation between rotation turns and time, plotted as a function of time (Fig. 2C). As the twisted fiber untwists, the rotation rate initially increases and reaches a peak value within a few seconds before gradually decreasing to zero. The behavior of fiber-shaped micromotors might correlate with their mechanical properties regulated by UV exposures. Specifically, as the UV curing time was extended from 30 to 40 s, the as-printed fibers exhibited an increase in the rotation rate. However, when the exposure time was further increased to 50 s, the rotation rate showed a decreasing trend. The fiber cured for 40 s achieved the highest top rotating speed of 314 rpm and the shortest acceleration/recovery time (Fig. 2D), probably due to a good balance between modulus and toughness (Fig. 1D). In contrast, the fiber cured for the longest time (50 s) attained a lower top speed of 109 rpm, despite having the maximum modulus of the fiber material (Fig. S7). Thus, co-regulations of the modulus and toughness may optimize the rotation motions. Furthermore, we programmed more twisting turns (*e.g.*, 300 turns m^{-1}) to increase the stored torsional mechanical energy for fibers curing at 35 and 40 s. The best-performing SMP fiber (40 s) can achieve a higher maximum rotation rate (*e.g.*, 350 rpm) (Figs. S8 and S9).

In addition to the curing time dependence, we explored the impact of temperature on the torsional twist behavior of our fiber-shaped micromotors. Fig. 2E and F present the untwisting rotation performance of SMP fibers at three different temperatures (45, 60, and 75 °C). At low temperatures of 45 and 60 °C, the twisted SMP fibers exhibited slower

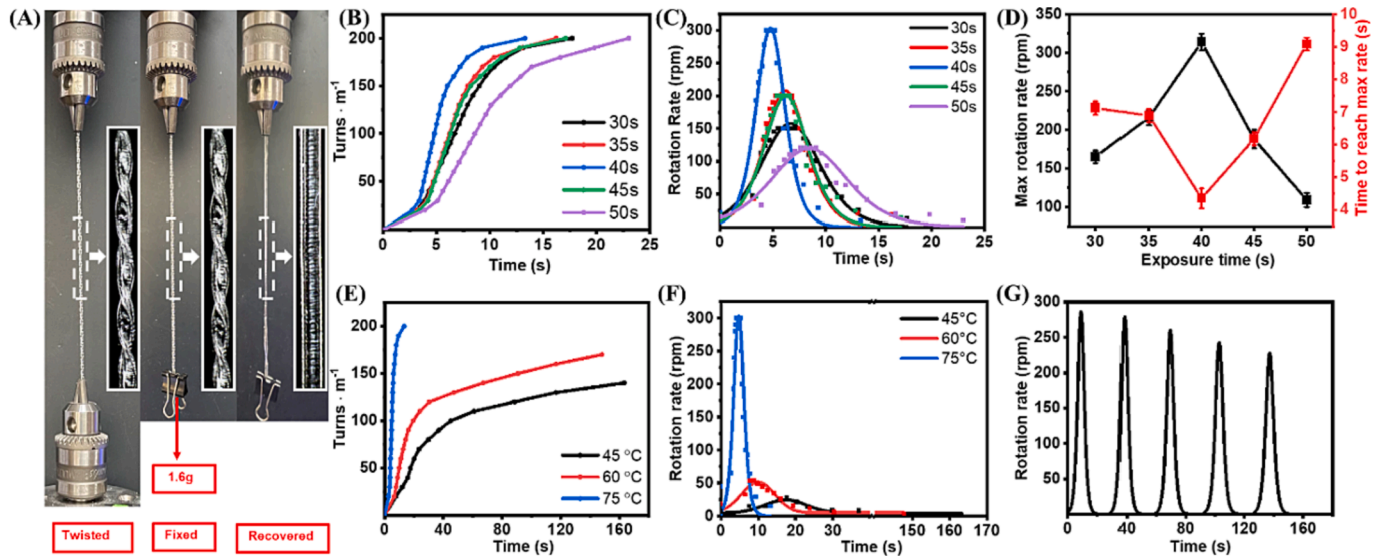

Fig. 2. Thermal responsive behaviors of SMP fiber-shaped micromotor printed layer-by-layer at different exposure times (30, 35, 40, 45, and 50 s). A) Illustration of the SMP programming process from the twisted state, programmed (fixed) state, to the recovered state. B) The rotation turns versus time. C) The rotation rate (rpm) as a function of time is obtained from the first derivative of the correlation in (B). D) Maximum rotation rate and time to reach the top rate versus exposure time. E) Rotation turns versus time of as-printed fiber (40 s exposure time) programming under different temperatures (45, 60, and 75 °C). F) Rotation rate versus time of SMP fiber under different programming temperatures. G) Repeatedly programming (5 cycles) SMP fibers at 75 °C.

rotation motions, with reduced maximum rates of 50 and 25 rpm, respectively, compared to a top speed of 300 rpm for the fiber untwisted at 75 °C. The fibers tested at low temperatures also took longer to recover to their original state. Furthermore, the fibers tested at lower temperatures only achieved recoveries of 170 turns m^{-1} at 60 °C and 140 turns m^{-1} at 45 °C, resulting in relatively lower shape recovery ratios of 85 % and 70 %, respectively (Table S2), compared to 100 % shape recovery ratio for the fiber untwisted at 75 °C with the same programmed rotation turns (*e.g.*, 200 turns m^{-1}). Moreover, temperature significantly influences our SMP fibers' mechanical characteristics, as evidenced by the stress-strain curves (Figs. S10-S12). As the programming temperature increases and surpasses T_g, a softening effect becomes apparent due to the phase transition from a glassy state to a rubbery state, leading to reductions in both Young's modulus and ultimate strength. To explore the optimal programming temperature, we measured the generated torque of a twisted fiber (*e.g.*, cured with an exposure time of 40 s) via DMA with both ends tethered while reheating it from room temperature to 110 °C (Fig. S13). This analysis reveals an optimal programming temperature as we approach T_g, where SMP generates the maximum torque value of 0.075 mM·m at 69.5 °C. In addition, we demonstrated the reversibility of our SMP fiber motors through five sequential programming/reprogramming cycles (Fig. 2G), showing a slight decrease in the maximum rotation rate while maintaining a nearly 100 % shape recovery ratio (Figs. S14 and S15).

3.3. Grayscale lithography-regulated heterogeneous domains

Based on the fundamental studies demonstrated in the previous sections, we developed a novel approach to incorporate heterogeneous domains, thereby generating multiple advantages within a single SMP material, which enables the regulation of global properties. This approach grants us additional control over the responsive behaviors within a single SMP actuator. Specifically, we employed a grayscale lithography technique to introduce heterogeneous domains into our SMP fibers by controlling the spatial distribution profile of the localized curing times. The grayscale lithography was realized using a fixed-height UV curable system in a photo-stereolithography-based LCD 3D printer. Fig. S16 illustrates the basic configuration, which involves a closed secondary cell constructed inside the resin vat with spacers to constrain the height of the printing samples (0.6–0.9 mm). In this work, we printed three dog-bone specimens with different designed heterogeneous domains, as depicted by their 3D models in Fig. 3A, along with the corresponding distribution profiles of accumulated UV curing time shown in Fig. 3B. It is important to note that the thickness of the specimens is fixed by constructing a closed secondary cell inside the resin vat. The various thicknesses indicated in the printing models (Fig. 3A) do not represent the dimensions of the printing samples. Instead, they signify the number of curing times (*e.g.*, 25 s for each unit exposure in Fig. 3B), which can tune the material properties by varying the accumulated doses of UV exposure. To this end, we employed a series of dynamic masks to spatially control the UV curing at specific sites, thereby producing heterogeneous domains (Fig. 3C). To gain a deeper understanding of the mechanical behaviors influenced by the heterogeneous domains, we conducted a time-resolved strain mapping analysis using digital image correlation (DIC) during uniaxial tensile tests on the three dog-bone specimens with different designed heterogeneities (Fig. 3D, Movies S1-S3). We derived localized stress-strain curves at representative heterogeneous domains by correlating the strain mapping data from the DIC analysis with the corresponding stress obtained from the tensile test (Fig. 3E).

In our investigation, we integrated three distinct designs into our dog-bone specimens. The first design (Design 1: Hetero-t_1-t_5) involved a gradual increment in curing time, spanning from the short exposure of 50 s to a maximum of 150 s, with 25 s intervals. This configuration yielded a longitudinal stiffness gradient distributed between relatively soft (t_1 = 50 s) and stiff (t_5 = 150 s) domains (Fig. 3A1 and B1). In the second design (Design 2: Hetero-t_5@t_1-h), we alternated solely between minimum (t_1 = 50 s) and maximum exposure times (t_5 = 150 s) along the longitudinal direction. This led to distinct interfaces between stiff and soft domains (Fig. 3A2 and B2). For the third design (Design 3: Hetero-t_5@t_1-v), we explored the impact of domain orientation by aligning stiff domains vertically, parallel to the tensile stretch (Fig. 3A3, and B3). These SMPs with integrated heterogeneous domains exhibited slight variations in glass transition temperatures, as determined through DMA (Figs. S17-S20).

We employed DIC analysis to conduct strain mapping, thereby gaining deeper insight into the localized mechanical properties at specific heterogeneous domains. Representative regions were selected to

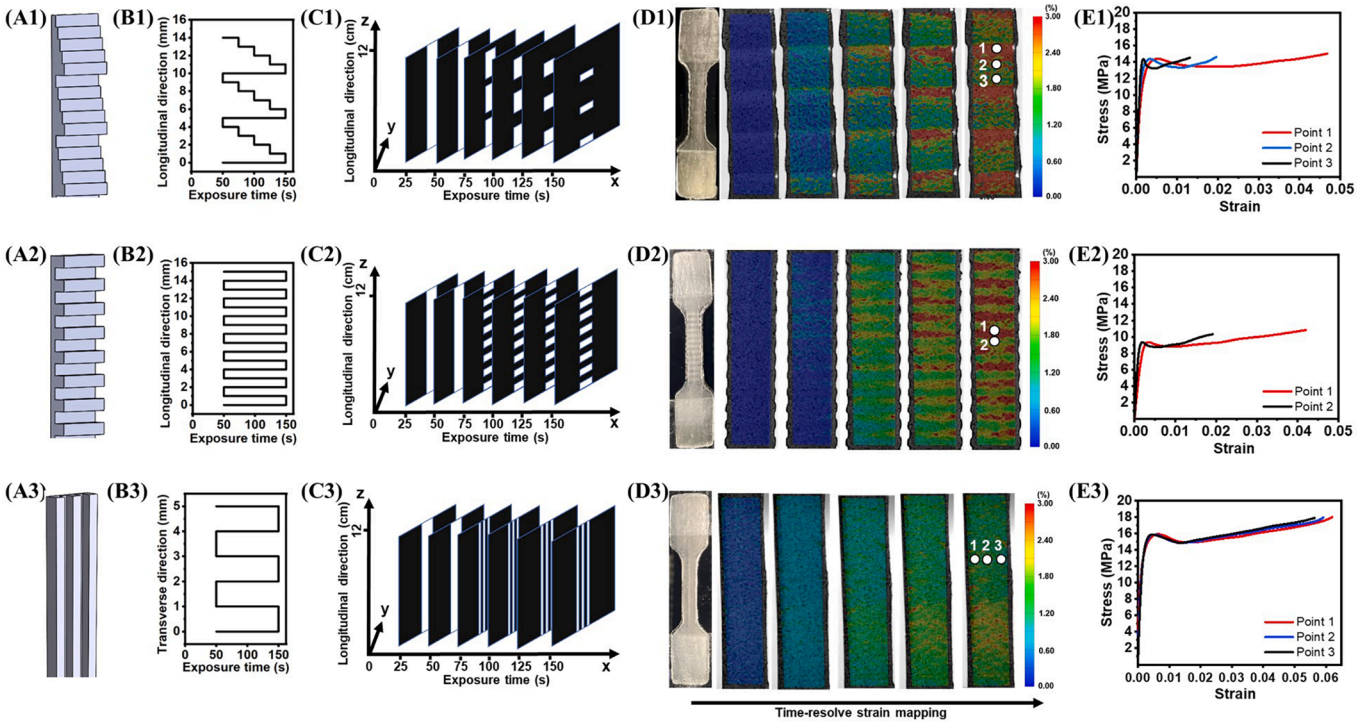

Fig. 3. A grayscale lithography-regulated heterogeneous domains in dog-bone specimens. 3D model (A) and spatial distribution profiles of accumulated exposure time (B) for three designs of heterogeneous structures. C) The illustration of a series of dynamic masks to realize each design by spatially controlling the curing time in a fixed-height printing. D) The time-resolved strain mapping via digital image correlation (DIC) analysis under a uniaxial tensile test at room temperature for three dog-bone specimens with different designs. E) The stress-strain curves of representative localized heterogeneous domains obtained from DIC analysis. Hetero-t_1-t_5: exposure time gradually increasing from t_1 to t_5 along the longitudinal direction ($t_1 = 50$ s, $t_2 = 75$ s, $t_3 = 100$ s, $t_4 = 125$ s, $t_5 = 150$ s); Hetero-t_5@t_1-h: exposure time alternatively changing between t_1 and t_5 along the longitudinal direction; Hetero-t_5@t_1-v: exposure time alternatively changing between t_1 and t_5 along the lateral direction.

monitor heterogeneous mechanical behaviors within the three designed specimens. As depicted in Fig. 3D, relatively stiff areas displayed minor localized deformations and strains compared to their relatively soft counterparts. For instance, in Design 1, strains at representative stiff (point 3), soft (point 1), and intermediate regions (point 2) were easily distinguishable through time-resolved strain variations. Corresponding localized stress-strain curves for the three selected regions are presented in Fig. 3E1. These curves reveal a progressive increase in modulus (*e.g.*, $E_1 < E_2 < E_3$), ranging from 623 to 982 MPa, alongside a reduction in strain to failure (*e.g.*, $\varepsilon_1 > \varepsilon_2 > \varepsilon_3$). Consequently, the single specimen encoded with heterogeneous domains showcased a gradient in modulus. In Design 2, a stark shift between soft and stiff domains is evident, with substantial strain disparities between selected points 1 and 2 ($\varepsilon_1 > \varepsilon_2$), indicating a sharp transition in modulus at interfaces. Conversely, in Design 3, no discernible differences in stress-strain behaviors were observed across different regions. This outcome is attributed to the alignment of stiff domains parallel to the tensile stretch, resulting in concentrated stress within stiff regions to carry the load. As a result, similar modulus values (*e.g.*, 1083, 1057, 1042 MPa) were measured in three different localized regions (points 1–3), irrespective of stiff and soft domains. Furthermore, the specimen featuring vertically aligned stiff domains exhibited higher ultimate strength than the other two designs (*e.g.*, 16 versus 14 or 9 MPa).

3.4. Engineering heterogeneities for co-regulations of responsive rotations and mechanical properties

To further explore the heterogeneities in fiber-shaped actuators, we replicated three designs to encode our fiber-shaped micromotors with a dimension of 0.9 mm × 0.9 mm × 120 mm via a fixed height grayscale lithography technique (Fig. 4A and Fig. S16). Initially, we fabricated five homogeneous fibers with different curing times (Homo-t_1: 50 s, Homo-t_2: 75 s, Homo-t_3: 100 s, Homo-t_4: 125 s, and Homo-t_5: 150 s) as control samples (Table S4). The increase in curing time from 50 to 150 s resulted in a more than four-fold increase in Young's modulus, ranging from 265 to 1208 MPa for the homogeneous fibers (Fig. 4B and Fig. S21). Meanwhile, the maximum rotation rate of these fibers also varied, starting from 196 rpm (Homo-t_1: 50 s curing time) with a relatively longer acceleration time, reaching a peak value of 366 rpm (Homo-t_3: 100 s curing time) with the shortest time to reach the top rate (Movie S4), and eventually decreasing to 169 rpm (Homo-t_5: 150 s) with prolonged acceleration time (Fig. 4C, Figs. S22 and S23; Movie S5). This trend follows a similar variation pattern observed in the layer-by-layer printing approach (Fig. 2D).

Compared to homogeneous fibers, our designed heterogeneous fibers exhibit simultaneous regulations of mechanical properties and stimuli-responsive performance. Here, the programming temperature of 75 °C was selected based on the glass transition temperatures of the three heterogeneous fibers (Figs. S17-S20). By incorporating various stiff (*e.g.*, 150 s) and soft domains (*e.g.*, 50 s) into our fiber-shaped actuators, the as-fabricated fibers with three designs demonstrate a tunable modulus ranging from 885 to 1063 MPa while controlling the rotation motion. Specifically, the Hetero-t_5@t_1-h fiber with horizontal domains that alternatively change between the lowest curing time t_1 and the highest curing time t_5 along the fiber direction, features sharp stiff (t_5)-soft (t_1) interfaces (Design 2). This Hetero-t_5@t_1-h fiber exhibits an intermediate Young's modulus compared to the soft Homo-t_1 fiber (*e.g.*, 265 MPa) and stiff Homo-t_5 fiber (*e.g.*, 1208 MPa) due to the integration of stiff and soft domains. By taking advantage of both relatively soft and relatively stiff domains, Hetero-t_5@t_1-h fiber shows a maximum rotation rate of 258 rpm (Movie S6), which is higher than its homogeneous counterparts (*e.g.*, 196 rpm for Homo-t_1 fiber; 169 rpm for Homo-t_5 fiber). As a result,

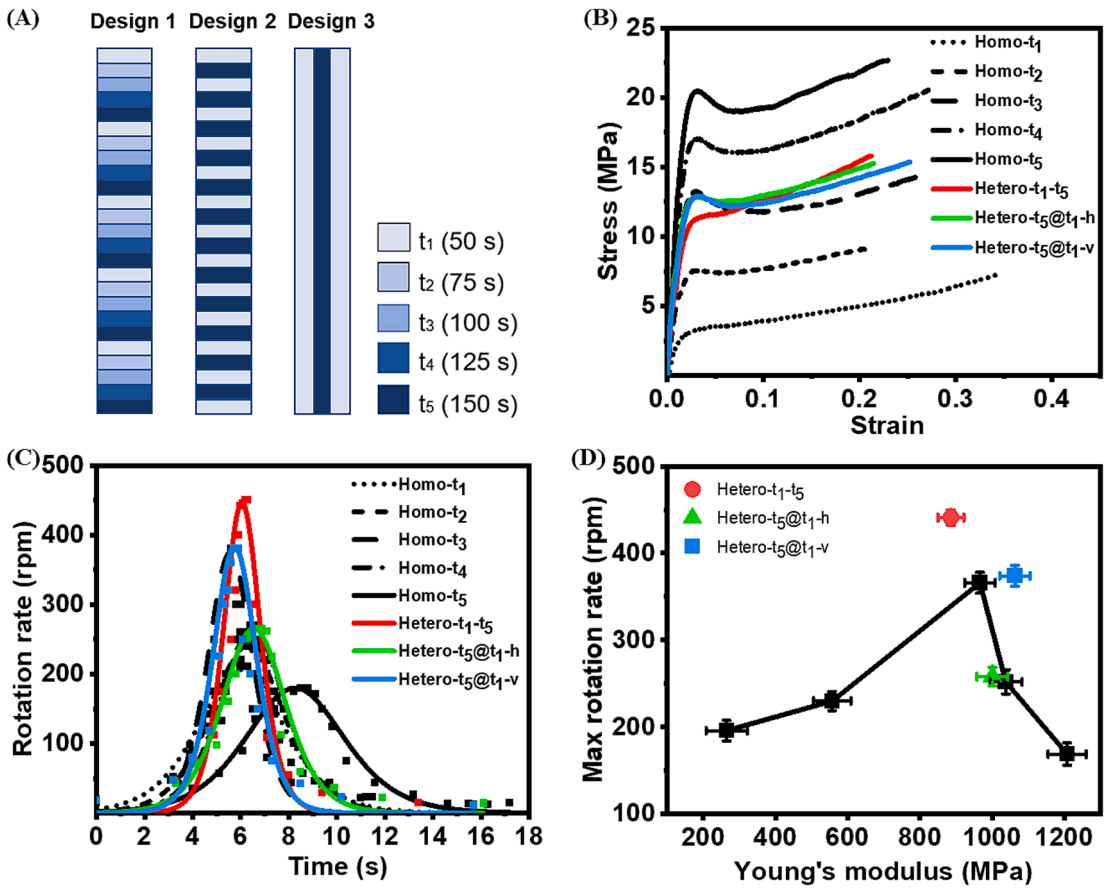

Fig. 4. Characteristics of fiber-shaped actuators with three designed heterogeneous domains. A) Schematic illustration of three designs. B) Stress–strain curves of fibers with three designs (*e.g.*, Design 1: Hetero-t_1-t_5; Design 2: Hetero-t_5@t_1-h; Design 3: Hetero-t_5@t_1-v) and homogeneous fibers as the control samples (*e.g.*, Homo-t_1: 50 s; Homo-t_2: 75 s, Homo-t_3: 100 s; Homo-t_4: 125 s, and Homo-t_5: 150 s). C) The rotation rate (rpm) as a function of time obtained from the first derivative of time-dependent rotation turns tested at 75 °C. D) The correlation of Young's modulus and maximum rotation rate for homogenous (black symbols) and heterogenous fiber-shaped actuators.

the sharp variation at the interfaces between the stiff and soft domains enhances the stimuli-responsive performance.

Moreover, the orientation of the heterogeneous domains significantly influences the rotational performance of the fiber-shaped micromotor. Specifically, the Hetero-t_5@t_1-v fiber, featured by strengthened stiff domains along the longitudinal direction, exhibits an impressive maximum rotation rate of 374 rpm, outperforming the Hetero-t_5@t_1-h fiber. This enhanced performance is likely attributed to the presence of reinforced stiff domains that align with the fiber's direction. In addition, the Hetero-t_1-t_5 fiber presents an intriguing structure, incorporating a gradient of stiffness modulus achieved through spatial designs (such as t_2-t_3-t_4) between its stiffest (cured at t_5) and softest (cured at t_1) domains. Impressively, this fiber with a heterogeneous gradient achieves an even higher maximum rotation rate of 441 rpm (refer to Movie S7) compared to the other two heterogeneous fibers studied. This notable enhancement can be attributed to the gradient characteristics existing between the stiff and soft domains. This gradient feature synergistically combines the complementary properties of adjacent domains, akin to the heterogeneous gradients observed in various natural organisms. Consequently, the strategic introduction of heterogeneous domains within a single fiber-shaped actuator presents a novel and effective approach for simultaneously co-regulating overall mechanical properties and stimuli-responsive behaviors.

3.5. Regulated mechanical energy of torsional actuators with designed heterogeneities

To further investigate the stored and released mechanical energy of our torsional actuators as rotating micromotors, we fabricated a hybrid fiber consisting of two regions with a total length of 7.0 cm, as shown in Fig. 5A. The upper region, which is 3.5 cm long, serves as a rotating micromotor against an applied torque, while the lower region, also 3.5 cm in length, acts as a torque load (Fig. 5B). In the first step, we tethered only the two ends of the upper motor region, as indicated by the red triangles (Fig. 5A). Then, the upper region was programmed to store torsional mechanical energy by twisting it with 10 turns at T_d ~75 °C. Subsequently, the hybrid fiber was quenched at room temperature, keeping the upper motor region fixed in a twisted state while the lower end remained untethered (step 2). Upon reheating the entire hybrid fiber, which was tethered at both ends (step 3), the stored torsional mechanical energy in the upper region was released, enabling it to function as a rotating micromotor. The micromotor could rotate and overcome the increasing torsional load generated by the lower region as it continued to be twisted. Hence, the upper micromotor can exert work capacity to counteract the growing load imposed by the lower region.

To ensure the proper selection and integration of a motor and a load in a hybrid fiber, we first measured and compared the torques required to twist five candidates, including three heterogeneous fibers and two homogenous fibers, by 285 turns m^{-1} at T_d (Fig. 5C). Consistent with our findings on rotation motions (Fig. 4C), the Hetero-t_1-t_5 fiber, featuring a heterogeneous gradient between the stiffest and softest domains,

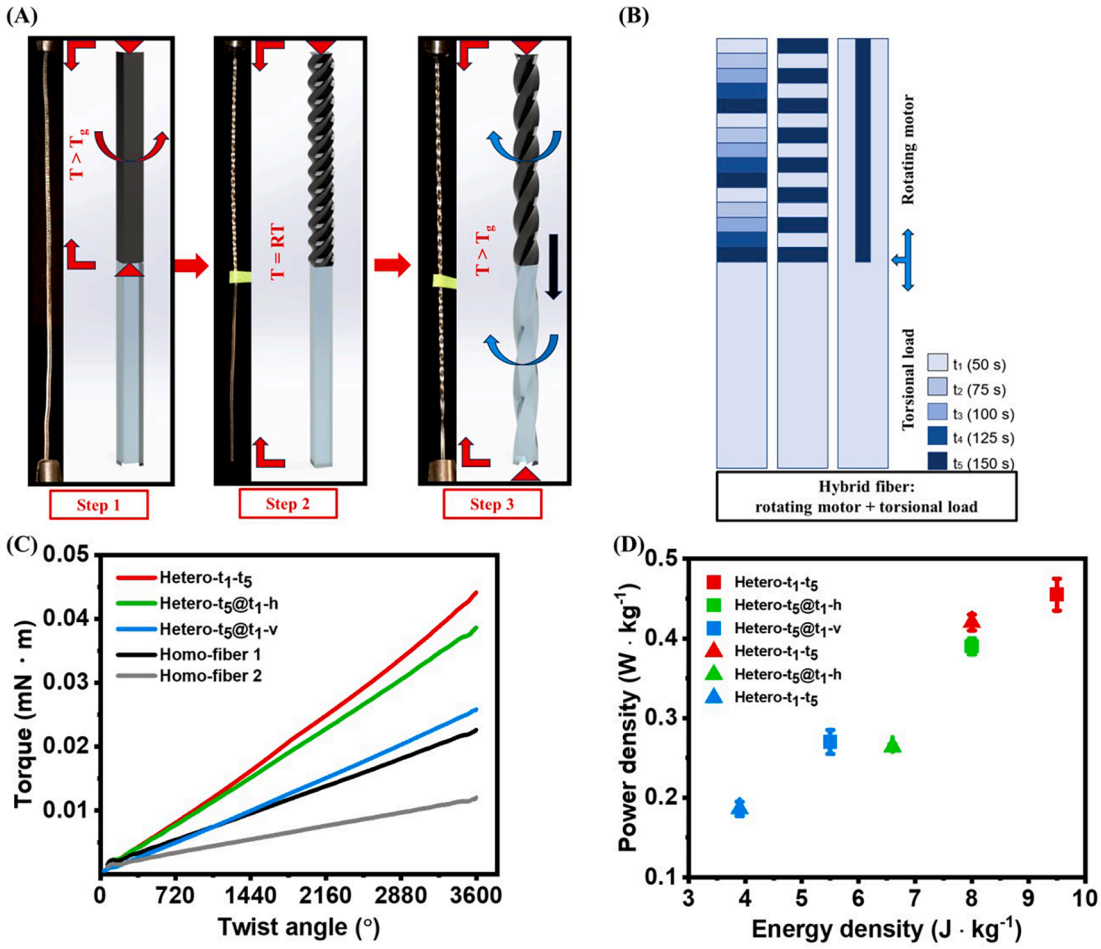

Fig. 5. Stored/released mechanical energy of torsional fiber-shaped actuators with designed heterogeneities. A) The illustration of a three-step process to measure the output torsional mechanical energy: step 1 twist/program the upper region with two ends tethered to store torsional mechanical energy at $T_d \sim 75$ °C; step 2 quench the entire hybrid fiber at room temperature to keep the upper region fixed in a twisted state with only the top end tethered; step 3 tether two ends of the entire fiber and reheat it at T_d to release the stored mechanical energy in the upper region, which can rotate the lower region to overcome the increasing torsional load generated as the lower region is twisted. The red triangle indicates tethered end(s); the red curved arrow indicates programmed rotation direction; the blue curved arrow indicates released rotation direction. B) Schematic illustration of hybrid fibers consisting of the upper region with designed heterogeneities as a rotating motor (*e.g.*, Design 1: Hetero-t_1-t_5; Design 2: Hetero-t_5@t_1-h; Design 3: Hetero-t_5@t_1-v) and the lower homogenous region as a torsional load (*e.g.*, Homo-fiber 1: printed at 50 s; Homo-fiber 2: printed at 25 s). C) Torque needed to twist three heterogeneous fibers and two homogenous fibers by 285 turns m^{-1} at T_d (3.5 cm in length). D) Power density versus energy density of rotating motors with designed heterogeneous domains against various torsional loads generated by Homo-fiber 1 (square symbol) and Homo-fiber 2 (triangle symbol). (For interpretation of the references to colour in this figure legend, the reader is referred to the web version of this article.)

exhibited the highest torque deliveries with the twisted angles (Fig. 5C). Notably, all three heterogeneous fibers showed higher torques than the two homogeneous fibers. Moreover, the act of programming and untwisting the fiber for energy storage and release showcased highly reversible characteristics, as evident by the torque-angle curves (Fig. S24). This behavior can be attributed to the notably high shape recovery ratio exhibited by our SMP fibers.

We calculated the torsional mechanical energies of these fiber-shaped micromotors by integrating the torque-angle curves using the formula $U = \Gamma \int d\theta$, where Γ represents the measured torque and θ denotes the rotation angle. Upon programming 285 turns m^{-1}, the three heterogeneous fibers stored torsional energies of 69, 59.5, and 41.5 J kg^{-1} for designs 1–3, respectively, surpassing the stored energies of the two homogeneous fibers (*e.g.*, 34.5 J kg^{-1} for Homo-fiber 1 and 19 J kg^{-1} for Homo-fiber 2) (Table S5). Given their relatively high torques and mechanical energies, we selected heterogeneous fibers serving as micromotors and homogeneous fibers as the torsional load. Specifically, we printed one designed heterogeneous pattern in the upper region of the hybrid fiber as a rotating micromotor for storing and releasing torsional energies, and encoded a homogeneous photo-polymerization to the lower region of the hybrid fiber as torsional loads. For example, the Hetero-t_1-t_5 micromotor is positioned in the upper segment of the hybrid fiber. This micromotor facilitates distinct energy outputs by inducing varying torque values while causing the rotation of homogeneous fibers. The Hetero-t_1-t_5 micromotor effectively drives the rotation of Homo-fiber 1 and Homo-fiber 2 loads, completing 5 and 6.5 revolutions, respectively, as the twisting process continues. The mechanical energy (work capacity) generated from the Hetero-t_1-t_5 micromotor in the upper region (0.02 g) was calculated to be 9.5 J kg^{-1} (power density: 0.45 W kg^{-1}) when subjected to high load twisting (Homo-fiber 1) (Fig. 5D and Fig. S25). Against the low load (Homo-fiber 2), the micromotor delivered a work capacity of 8.0 J kg^{-1} (power density: 0.42 W kg^{-1}). The other two heterogeneous micromotors exhibited slightly lower energy and power outputs (*e.g.*, Hetero-t_5@t_1-h: 8.0/6.5 J kg^{-1} for high/low load; Hetero-t_5@t_1-v: 5.5/3.9 J kg^{-1} for high/low load). Moreover, the ratio of released energy to stored energy for the Hetero-t_1-t_5 fiber was calculated to be 13.76 %, indicating a high output energy efficiency, which surpasses that of other torsional fiber actuators reported in the previous literature (Table S6). It is worth noting that our torsional actuators can deliver significantly higher torque, energy

density, and power density compared to previously reported actuators [1,43–49]. However, the performance normalized by weight (*e.g.*, specific torque, specific energy density, and specific power density) is substantially degraded due to the much larger diameter of our printed fibers (~900 μm vs. 10–40 μm), limited by the resolution of the printer and light scattering during the printing process. The fiber diameter inversely scales with torsional stroke, thus critically impacting the fiber twist and energy/power outputs. In our future work, we intend to fabricate smaller-diameter fibers by employing high-resolution micro-stereolithography, favoring larger strokes, higher rotation rates, and higher stored/released mechanical energy.

4. Conclusion

Our work introduces a novel strategy for fabricating intelligent materials or actuators. The creation of heterogeneous domains differs from the composite concept of integrating dissimilar materials, such as reinforced inclusions in a composite. In our study, we spatially control the site-specific photo-polymerization of the resin precursor during a gray-scale lithography-enabled printing process to fabricate diverse heterogeneous domains within a single material. This allows us to regulate gradients, orientations, and crosslinking, enabling the tuning of global properties of the fabricated actuators. As a result, the technique we developed empowers the encoding of photo-sensitive resins with spatially regulated material properties and responsive performance in the fiber-shaped SMP actuators. This approach goes beyond mere control of printed geometry. Consequently, our strategy, characterized by the incorporation of heterogeneous domains and transition interfaces, opens a pioneering avenue for designing and fabricating intelligent materials and associated actuation devices, thereby expanding their applications across diverse domains.

CRediT authorship contribution statement

Zhongkun Zhao: Formal analysis, Investigation, Methodology, Visualization, Writing – original draft. **Haoqing Yang:** Formal analysis, Investigation, Methodology. **Manqi Li:** Investigation, Methodology, Validation. **Chandan Gudi:** Validation, Writing – review & editing. **Kamal Varma Kanumuru:** . **Robert Voigt:** Writing – review & editing. **Olalekan Babaniyi:** Writing – review & editing. **Tengxiao Liu:** Conceptualization, Methodology, Supervision, Writing – original draft. **Yong Chen:** Methodology, Supervision, Writing – review & editing. **Hongtao Sun:** Conceptualization, Formal analysis, Funding acquisition, Project administration, Resources, Supervision, Writing – original draft.

Declaration of competing interest

The authors declare that they have no known competing financial interests or personal relationships that could have appeared to influence the work reported in this paper.

Data availability

Data will be made available on request.

Acknowledgement

H. Sun would like to thank the Pennsylvania State University start-up fund for supporting this work.

Appendix A. Supplementary data

Supplementary data to this article can be found online at https://doi.org/10.1016/j.cej.2023.147936.

References

[1] J. Yuan, W. Neri, C. Zakri, P. Merzeau, K. Kratz, A. Lendlein, P. Poulin, Shape memory nanocomposite fibers for untethered high-energy microengines, Science. 365 (2019) 155–158, https://doi.org/10.1126/science.aaw3722.
[2] M. Su, Y. Song, Printable smart materials and devices: strategies and applications, Chemical Reviews. 122 (2021) 5144–5164, https://doi.org/10.1021/acs.chemrev.1c00303.
[3] Z. Zhu, D.W.H. Ng, H.S. Park, M.C. McAlpine, 3D-printed multifunctional materials enabled by artificial-intelligence-assisted fabrication technologies, Nature Reviews Materials. 6 (2021) 27–47, https://doi.org/10.1038/s41578-020-00235-2.
[4] Z. Lou, L. Wang, G. Shen, Recent advances in smart wearable sensing systems, Advanced Materials Technologies. 3 (2018) 1800444, https://doi.org/10.1002/admt.201800444.
[5] J. Gardan, Smart materials in additive manufacturing: state of the art and trends, Virtual and Physical Prototyping. 14 (2019) 1–18, https://doi.org/10.1080/17452759.2018.1518016.
[6] X. Qiu, S. Hu, "Smart" materials based on cellulose: a review of the preparations, properties, and applications, Materials. 6 (2013) 738–781, https://doi.org/10.3390/ma6030738.
[7] M. Stoppa, A. Chiolerio, Wearable electronics and smart textiles: A critical review, Sensors. 14 (2014) 11957–11992, https://doi.org/10.3390/s140711957.
[8] L. Peponi, I. Navarro-Baena, A. Sonseca, E. Gimenez, A. Marcos-Fernandez, J. M. Kenny, Synthesis and characterization of PCL–PLLA polyurethane with shape memory behavior, European Polymer Journal. 49 (2013) 893–903, https://doi.org/10.1016/j.eurpolymj.2012.11.001.
[9] P. Miaudet, A. Derre, M. Maugey, C. Zakri, P.M. Piccione, R. Inoubli, P. Poulin, Shape and temperature memory of nanocomposites with broadened glass transition, Science. 318 (2007) 1294–1296, https://doi.org/10.1126/science.1145593.
[10] T. Chung, A. Romo-Uribe, P.T. Mather, Two-way reversible shape memory in a semicrystalline network, Macromolecules. 41 (2008) 184–192, https://doi.org/10.1021/ma071517z.
[11] J. Li, W.R. Rodgers, T. Xie, Semi-crystalline two-way shape memory elastomer, Polymer. 52 (2011) 5320–5325, https://doi.org/10.1016/j.polymer.2011.09.030.
[12] L. Yu, H. Shahsavan, G. Rivers, C. Zhang, P. Si, B. Zhao, Programmable 3D shape changes in liquid crystal polymer networks of uniaxial orientation, Advanced Functional Materials. 28 (2018) 1802809, https://doi.org/10.1002/adfm.201802809.
[13] W.-G. Drossel, H. Kunze, A. Bucht, L. Weisheit, K. Pagel, Smart3–Smart materials for smart applications, Procedia Cirp. 36 (2015) 211–216, https://doi.org/10.1016/j.procir.2015.01.055.
[14] L. Wang, Y. Jian, X. Le, W. Lu, C. Ma, J. Zhang, Y. Huang, C.-F. Huang, T. Chen, Actuating and memorizing bilayer hydrogels for a self-deformed shape memory function, Chemical Communications. 54 (2018) 1229–1232, https://doi.org/10.1039/C7CC09456F.
[15] Q. Zhao, H.J. Qi, T. Xie, Recent progress in shape memory polymer: New behavior, enabling materials, and mechanistic understanding, Progress in Polymer Science. 49 (2015) 79–120, https://doi.org/10.1016/j.progpolymsci.2015.04.001.
[16] A. Lendlein, M. Balk, N.A. Tarazona, O.E. Gould, Bioperspectives for shape-memory polymers as shape programmable, active materials, Biomacromolecules. 20 (2019) 3627–3640, https://doi.org/10.1021/acs.biomac.9b01074.
[17] Y. Wang, Y. Miao, J. Zhang, J.P. Wu, T.B. Kirk, J. Xu, D. Ma, W. Xue, Three-dimensional printing of shape memory hydrogels with internal structure for drug delivery, Materials Science and Engineering: c. 84 (2018) 44–51, https://doi.org/10.1016/j.msec.2017.11.025.
[18] L. Sun, W.M. Huang, Z. Ding, Y. Zhao, C.C. Wang, H. Purnawali, C. Tang, Stimulus-responsive shape memory materials: a review, Materials & Design. 33 (2012) 577–640, https://doi.org/10.1016/j.matdes.2011.04.065.
[19] Y. Liu, H. Du, L. Liu, J. Leng, Shape memory polymers and their composites in aerospace applications: a review, Smart Materials and Structures. 23 (2014), 023001, https://doi.org/10.1088/0964-1726/23/2/023001.
[20] L. Wang, F. Zhang, Y. Liu, J. Leng, Shape memory polymer fibers: materials, structures, and applications, Advanced Fiber Materials. (2022) 1–19, https://doi.org/10.1007/s42765-021-00073-z.
[21] J. Hu, H. Meng, G. Li, S.I. Ibekwe, A review of stimuli-responsive polymers for smart textile applications, Smart Materials and Structures. 21 (2012), 053001, https://doi.org/10.1088/0964-1726/21/5/053001.
[22] Y. Xia, Y. He, F. Zhang, Y. Liu, J. Leng, A review of shape memory polymers and composites: mechanisms, materials, and applications, Advanced Materials. 33 (2021) 2000713, https://doi.org/10.1002/adma.202000713.
[23] M.H. Godinho, J.P. Canejo, G. Feio, E.M. Terentjev, Self-winding of helices in plant tendrils and cellulose liquid crystal fibers, Soft Matter. 6 (2010) 5965–5970, https://doi.org/10.1039/C0SM00427H.
[24] M.H. Godinho, J.P. Canejo, L.F.V. Pinto, J.P. Borges, P.I.C. Teixeira, How to mimic the shapes of plant tendrils on the nano and microscale: spirals and helices of electrospun liquid crystalline cellulose derivatives, Soft Matter. 5 (2009) 2772–2776, https://doi.org/10.1039/B821631B.
[25] S.J. Gerbode, J.R. Puzey, A.G. McCormick, L. Mahadevan, How the cucumber tendril coils and overwinds, Science. 337 (2012) 1087–1091, https://doi.org/10.1126/science.1223304.
[26] Y. Cheng, R. Wang, K.H. Chan, X. Lu, J. Sun, G.W. Ho, A biomimetic conductive tendril for ultrastretchable and integratable electronics, muscles, and sensors, ACS Nano. 12 (2018) 3898–3907, https://doi.org/10.1021/acsnano.8b01372.

[27] W. Wei, J. Liu, J. Huang, F. Cao, K. Qian, Y. Yao, W. Li, Recent advances and perspectives of shape memory polymer fibers, European Polymer Journal. (2022), 111385, https://doi.org/10.1016/j.eurpolymj.2022.111385.
[28] G. Li, O. Ajisafe, H. Meng, Effect of strain hardening of shape memory polymer fibers on healing efficiency of thermosetting polymer composites, Polymer. 54 (2013) 920–928, https://doi.org/10.1016/j.polymer.2012.12.046.
[29] F. Ji, Y. Zhu, J. Hu, Y. Liu, L.-Y. Yeung, G. Ye, Smart polymer fibers with shape memory effect, Smart Materials and Structures. 15 (2006) 1547, https://doi.org/10.1088/0964-1726/15/6/006.
[30] Q. Yang, J. Fan, G. Li, Artificial muscles made of chiral two-way shape memory polymer fibers, Applied Physics Letters. 109 (2016), 183701, https://doi.org/10.1063/1.4966231.
[31] C.S. Haines, N. Li, G.M. Spinks, A.E. Aliev, J. Di, R.H. Baughman, New twist on artificial muscles, Proceedings of the National Academy of Sciences. 113 (2016) 11709–11716. https://doi.org/10.1073/pnas.1605273113.
[32] J. Mu, M. Jung de Andrade, S. Fang, X. Wang, E. Gao, N. Li, S.H. Kim, H. Wang, C. Hou, Q. Zhang, Sheath-run artificial muscles, Science. 365 (2019) 150–155, https://doi.org/10.1126/science.aaw2403.
[33] M. Kanik, S. Orguc, G. Varnavides, J. Kim, T. Benavides, D. Gonzalez, T. Akintilo, C.C. Tasan, A.P. Chandrakasan, Y. Fink, Strain-programmable fiber-based artificial muscle, Science. 365 (2019) 145–150, https://doi.org/10.1126/science.aaw2502.
[34] Y. Yao, Y. Xu, B. Wang, W. Yin, H. Lu, Recent development in electrospun polymer fiber and their composites with shape memory property: a review, Pigment & Resin Technology. (2018), https://doi.org/10.1108/PRT-04-2017-0039.
[35] Y. Zhang, L. Huang, H. Song, C. Ni, J. Wu, Q. Zhao, T. Xie, 4D printing of a digital shape memory polymer with tunable high performance, ACS Applied Materials & Interfaces. 11 (2019) 32408–32413, https://doi.org/10.1021/acsami.9b11062.
[36] Q. Ge, Z. Li, Z. Wang, K. Kowsari, W. Zhang, X. He, J. Zhou, N.X. Fang, Projection micro stereolithography based 3D printing and its applications, International Journal of Extreme Manufacturing. 2 (2020), 022004, https://doi.org/10.1088/2631-7990/ab8d9a.
[37] X. Kuang, J. Wu, K. Chen, Z. Zhao, Z. Ding, F. Hu, D. Fang, H.J. Qi, Grayscale digital light processing 3D printing for highly functionally graded materials, Science, Advances. 5 (2019) eaav5790, https://doi.org/10.1126/sciadv.aav5790.
[38] W. Shan, Y. Chen, M. Hu, S. Qin, P. Liu, 4D printing of shape memory polymer via liquid crystal display (LCD) stereolithographic 3D printing, Materials Research Express. 7 (2020), 105305, https://doi.org/10.1088/2053-1591/abbd05.
[39] A. Nojoomi, J. Jeon, K. Yum, 2D material programming for 3D shaping, Nature Communications 12 (2021) 603, https://doi.org/10.1038/s41467-021-20934-w.
[40] A. Nojoomi, H. Arslan, K. Lee, K. Yum, Bioinspired 3D structures with programmable morphologies and motions, Nature Communications 9 (2018) 3705, https://doi.org/10.1038/s41467-018-05569-8.
[41] K. Kowsari, B. Zhang, S. Panjwani, Z. Chen, H. Hingorani, S. Akbari, N.X. Fang, Q. Ge, Photopolymer formulation to minimize feature size, surface roughness, and stair-stepping in digital light processing-based three-dimensional printing, Additive Manufacturing. 24 (2018) 627–638, https://doi.org/10.1016/j.addma.2018.10.037.
[42] N. Fang, C. Sun, X. Zhang, Diffusion-limited photo-polymerization in scanning micro-stereolithography, Applied Physics a. 79 (2004) 1839–1842, https://doi.org/10.1007/s00339-004-2938-x.
[43] J. Foroughi, G.M. Spinks, G.G. Wallace, J. Oh, M.E. Kozlov, S. Fang, T. Mirfakhrai, J.D. Madden, M.K. Shin, S.J. Kim, Torsional carbon nanotube artificial muscles, Science. 334 (2011) 494–497, https://doi.org/10.1126/science.1211220.
[44] M.D. Lima, N. Li, M. Jung de Andrade, S. Fang, J. Oh, G.M. Spinks, M.E. Kozlov, C. S. Haines, D. Suh, J. Foroughi, Electrically, chemically, and photonically powered torsional and tensile actuation of hybrid carbon nanotube yarn muscles, Science. 338 (2012) 928–932, https://doi.org/10.1126/science.1226762.
[45] K.-Y. Chun, S. Hyeong Kim, M. Kyoon Shin, C. Hoon Kwon, J. Park, Y. Tae Kim, G. M. Spinks, M.D. Lima, C.S. Haines, R.H. Baughman, Hybrid carbon nanotube yarn artificial muscle inspired by spider dragline silk, Nature, Communications. 5 (2014) 3322, https://doi.org/10.1038/ncomms4322.
[46] P. Chen, Y. Xu, S. He, X. Sun, S. Pan, J. Deng, D. Chen, H. Peng, Hierarchically arranged helical fibre actuators driven by solvents and vapours, Nature Nanotechnology. 10 (2015) 1077–1083, https://doi.org/10.1038/nnano.2015.198.
[47] H. Cheng, Y. Hu, F. Zhao, Z. Dong, Y. Wang, N. Chen, Z. Zhang, L. Qu, Moisture-Activated Torsional Graphene-Fiber Motor, Adv. Mater. 26 (2014) 2909–2913, https://doi.org/10.1002/adma.201305708.
[48] S.M. Mirvakili, A. Pazukha, W. Sikkema, C.W. Sinclair, G.M. Spinks, R. H. Baughman, J.D. Madden, Niobium nanowire yarns and their application as artificial muscles, Advanced Functional Materials. 23 (2013) 4311–4316, https://doi.org/10.1002/adfm.201203808.
[49] W. Guo, C. Liu, F. Zhao, X. Sun, Z. Yang, T. Chen, X. Chen, L. Qiu, X. Hu, H. Peng, A novel electromechanical actuation mechanism of a carbon nanotube fiber, Advanced Materials. 24 (2012) 5379–5384, https://doi.org/10.1002/adma.201201845.